Journal of Solid State Chemistry 183 (2010) 807–813

Contents lists available at ScienceDirect

Journal of Solid State Chemistry

journal homepage: www.elsevier.com/locate/jssc

Experimental and theoretical studies of $Sn_{3-\delta}Pb_{\delta}Bi_2Se_6$ (δ=0.0–0.7)

Kuei-Bo Chen, Chi-Shen Lee *

Department of Applied Chemistry, National Chiao Tung University, 1001 University Road, Hsinchu 30010, Taiwan

ARTICLE INFO

Article history:
Received 6 October 2009
Received in revised form
31 December 2009
Accepted 9 January 2010
Available online 18 January 2010

Keywords:
Chalcogenide
Quaternary
Tin
Lead
Bismuth
Antimony
Selenide

ABSTRACT

New ternary and quaternary chalcogenides, $Sn_{3-\delta}Pb_{\delta}Bi_2Se_6$ (δ=0.0–0.7), were synthesized from pure elements using the solid-state method. Their crystal structures, determined using single crystal X-ray diffraction, belong to the orthorhombic space group *Pnma* (No. 62). The structure is related to $Pb_3Bi_2S_6$, which contains NaCl [311] layer units and zigzag arrays of metal atoms along the *c*-axis. A correlation between the Pb composition and the shifted position of a metal site was observed. Band structure calculations confirmed that the structure is stabilized when the position of the *M*5 site is farther from the mirror plane. Thermopower and conductivity measurements indicated that all of the compounds are n-type semiconductors with small band gaps.

1. Introduction

Post-transition-metal ions such as Bi^{3+} and Pb^{2+} often generate distorted coordination environments associated with the inert lone electron pair [1–3]. Chalcogenide compounds formed by combinations of such ions usually exhibit complex crystal structures and semiconducting properties with a narrow band gap, and are promising materials for nonlinear optics [4], ferroelectrics [5], and thermoelectrics [6–8]. Materials in this class contain various coordination environments constructed from M^{2+} (*M*=Sn, Pb) and M^{3+} (*M*=Sb, Bi) centers and Se^{2-} ions assembled into a structure similar to that of lillianite [9]. These structures are homologous, with ordered intergrowths of "NaCl- type" structures cut parallel to the (113) plane to form a number of diverse frameworks with chemically twinned arrangements, a current theme in crystal chemistry that has recently been reviewed [10–15]. The structures of the lillianite-type chalcogenides can be denoted as L(*n*,*n*′), in which *n* and *n*′ are the numbers of metal sites in the octahedral chains of the two alternating slabs; the different members of the lillianite series vary in the thickness of the NaCl-type blocks. Many naturally occurring minerals and synthetic lillianite-type or special case of Pavonite series [P(*N*,1)] chalcogenides have been studied, including $PbBi_4S_7$ [L(2,1)] [16]; $CuBi_5S_8$ [L(3,1)] [17]; $Cu_{3.21}Bi_{4.79}S_9$ [L(4,1)] [18]; $AgBi_3S_5$ [L(5,1)] [19]; $Pb_3Bi_2S_6$ [9,20], $AgPbBi_3S_6$ [21], and $AgPbSb_3S_6$ [L(4,4)] [22]; $Ag_5Pb_8Bi_{13}S_{30}$ [L(4,7)] [23]; $Pb_6Bi_2S_9$ [24] and $K_{0.54}Sn_{4.92}Bi_{2.54}Se_9$ [L(7,7)] [25]; $Ag_3Bi_7S_{12}$ [L(7,1)] [26]; $KSn_5Bi_5Se_{13}$ [L(4,5)] [25]; $Ag_7Pb_6Bi_{15}S_{32}$ [L(4,8)] [27]; $Ag_7Pb_{10}Bi_{15}S_{36}$ [L(5,9)] [10]; and $Ag_{12.5}Pb_{15}Bi_{20.5}S_{52}$ [L(11,11)] [11]. Most of the above lillianite and Pavonite type chalcogenides are sulfosalts; only a few selenides have been reported. Recently, we have demonstrated that multinary selenides, such as $InSn_2Bi_3Se_8$ [28], $In_{0.63}Sn_{5.57}Bi_{1.8}Se_9$ [28], $Pb_4In_xM_{6-x}Se_{13}$ [29] (*M*=Bi, *x*=2.1–2.8; Sb, *x*=2), $Sn_2Pb_5Bi_4Se_{13}$, and $Sn_{8.65}Pb_{0.35}Bi_4Se_{15}$ [30], can be prepared through solid-state synthetic routes that comprise various building units. Theoretical calculations have shown that the mixed occupancy metal sites arise from optimized *M*–Se bonding [29].

In this article, we present the synthesis and characterization of the lillianite-type selenides $Sn_{3-\delta}Pb_{\delta}Bi_2Se_6$ (δ=0.0–0.7). The structures of these as-synthesized phases are related to that of $Pb_3Bi_2S_6$, assigned to the space group *Bbmm* (No. 63), and contain a mirror plane between two NaCl [311] units with a mixed occupancy metal site on the mirror plane. Single-crystal analysis of these new phases identified a different space group, *Pnma* (No. 62), that contained a metal site close to the mirror plane. The reported lillianite phase $Pb_3Bi_2S_6$ [L(4, 4)] contains a metal site showing mirror symmetry. However, in these as-synthesized selenides, the corresponding metal site exhibits a zigzag array along the *c*-axis with glide symmetry. The percent composition of Pb was gradually changed to study the effects of Pb on the structure and coordination environments of metal sites. Electronic calculations were also carried out to evaluate the effects of the Pb^{2+} ion on the structure and coordination environments of the cations.

* Corresponding author. Fax: +886 3 5723764.
E-mail address: chishen@mail.nctu.edu.tw (C.-S. Lee).

0022-4596/$ - see front matter © 2010 Elsevier Inc. All rights reserved.
doi:10.1016/j.jssc.2010.01.011

2. Experiments

2.1. Synthesis

The elements were used as received: Sn powder, Alfa 99.5%; Bi power, Alfa 99.95%; Pb power, Alfa 99%; and Se powder, Alfa 99.9%. In a typical reaction, all compounds were obtained by heating a stoichiometric mixture of the elements in evacuated quartz tubes to 1073 K over 12 h, holding at 1073 K for 18 h, slow cooling to 773 K for 12 h, and then cooling to room temperature naturally.

2.2. Single-crystal X-ray diffraction (XRD)

Cuboid-shaped crystals obtained for $Sn_{3-\delta}Pb_\delta Bi_2Se_6$ [δ=0.0 (**1**), 0.1 (**2**), 0.3 (**3**), 0.5 (**4**), and x=0.7 (**5**)] were mounted on a glass fiber with epoxy glue for single-crystal X-ray diffraction analysis. Intensity data were collected using a diffractometer (Bruker APEX CCD equipped with graphite-monochromated Mo-$K\alpha$ radiation, λ=0.71073 Å) at 300 K. The crystal-to-detector distance was 5.038 cm and the exposure time was 30 s. Data were collected with a scan width of 0.3° in ω with four groups of 600 frames at ψ settings of 0°, 90°, 180°, and 270°. The 2θ values ranged between 1.76° and 56.54°. Diffraction peaks obtained from all frames of the reciprocal space images were integrated and used to determine the unit cell parameters using the Siemens SAINT program. The data were corrected for Lorentz and polarization effects using SADABS [31]. Absorption corrections were based on a function fitted to the empirical transmission surface sampled by multiple equivalent measurements of numerous reflections. The structural model was obtained using the direct method and refined by full-matrix least-squares refinement based on F^2 using the SHELXTL package [32].

All compounds had an orthorhombic lattice. Analysis of the systematic absence of reflections for compounds **1**–**3** suggested space group *Pnma* (No. 62). In the structural refinement process, a structural model was determined having five unique sites containing metal atoms (Sn, Bi, and Pb) and six unique sites containing Se atoms. The occupancy parameters were refined along with the displacement parameters. The results indicated that all Se sites were fully occupied and the *M*1–*M*5 sites had mixed occupancies. The refined electron counts of the *M*1–*M*5 sites were within 50–81 electrons/site, which were refined to fully occupied Sn (*M*3 site in compound 1) or mixed occupancy Sn/Bi or Sn/Pb sites. The final cycle of refinement included anisotropic displacement parameters and a secondary extinction correction performed on F^2. For compound **1**, the refinement of metal sites suffers from strong correlation between site occupancy and displacement parameter, which may be due to the poor X-ray diffraction data. The refinements indicate different electron densities in *M*1–*M*5 sites, and subsequently the site composition were estimated from the refined electron densities and fixed in the final stage of refinement. Fourier maps from **1**–**3** reveal residual peaks ~3.8–4.3 e$^-$/Å^3 close to *M*5 (~0.9 Å). The refined compositions for **1**–**3** were $(Sn^{+2})_3(Bi^{+3})_2(Se^{-2})_6$, $(Sn^{+2})_{2.93}(Pb^{+2})_{0.19}(Bi^{+3})_{1.89}(Se^{-2})_6$, and $(Sn^{+2})_{2.67}(Pb^{+2})_{0.32}(Bi^{+3})_2(Se^{-2})_6$, respectively, consistent with reaction stoichiometry.

Compounds **4** and **5** were initially refined with the C-centered space group *Cmcm* (No. 63), and structural refinements yielded reasonable values for *R*1/*wR*2 (**4**: 4.76%/11.85%, **5**: 3.07%/7.08%). However, the anisotropic displacement factors for the position on the mirror plane (*M*5 site) had unreasonable values (~0.181 and ~0.126 Å^2 along the *a*-axis for **4** and **5**, respectively). These values could reflect partially occupied Sn or Bi sites, but the refined formulae were not charge-balanced and did not justify this refinement. Ultimately, the *Pnma* space group was chosen and the assignments for the metal and Se sites were similar to those of **1**–**3**. The final refinements yielded charge-balanced formulae for **4** and **5** of $(Sn^{+2})_{2.49}(Pb^{+2})_{0.42}(Bi^{+3})_{2.09}(Se^{-2})_6$ and $(Sn^{+2})_{2.1}(Pb^{+2})_{0.67}(Bi^{+3})_{2.23}(Se^{-2})_6$, respectively.

Crystallographic data and selected bond distances for compounds **1**–**5** are given in Tables 1–3. Further details of the crystal-structure investigation can be obtained from Fachinformationszentrum

Table 1
Crystallographic data for $Sn_{3-\delta}Pb_\delta Bi_2Se_6$ (δ=0.0–0.7).

Empirical formula	$Sn_3Bi_2Se_6$	$Sn_{2.9}Pb_{0.1}Bi_2Se_6$	$Sn_{2.7}Pb_{0.3}Bi_2Se_6$	$Sn_{2.5}Pb_{0.5}Bi_2Se_6$	$Sn_{2.3}Pb_{0.7}Bi_2Se_6$
Refined formula	$Sn_3Bi_2Se_6$	$Sn_{2.93(6)}Pb_{0.19(3)}Bi_{1.89(5)}Se_6$	$Sn_{2.67(6)}Pb_{0.32(4)}Bi_{2.00(6)}Se_6$	$Sn_{2.49(4)}Pb_{0.42(2)}Bi_{2.09(4)}Se_6$	$Sn_{2.1(3)}Pb_{0.67(1)}Bi_{2.23(3)}Se_6$
Formula weight	1247.79	1256.64	1274.34	1292.04	1309.74
Temperature (K)			300(2)		
Wavelength (Å)			0.71073		
Crystal system			Orthorhombic		
Space group			*Pnma (No. 62)*		
Unit cell dimensions					
a	a=21.213(6) Å	*a*=21.373(4) Å	*a*=21.365(6) Å	*a*=21.399(8) Å	*a*=21.235(8) Å
b	b=4.162(1) Å	*b*=4.1898(8) Å	*b*=4.190(1) Å	*b*=4.190(2) Å	*b*=4.198(2) Å
c	c=13.640(4) Å	*c*=13.690(2) Å	*c*=13.741(4) Å	*c*=13.797(5) Å	*c*=13.846(6) Å
Volume (Å^3)	1204.2(6)	1226.0(4)	1230.2(6)	1239.7(8)	1234.3(9)
Z			4		
Density, calculated (mg/m^3)	6.883	6.808	6.881	6.923	7.048
Absorption coefficient (mm^{-1})	53.343	53.56	55.71	57.589	60.161
F(000)	2080	2092.8	2118.4	2144	2170
Crystal size (mm^3)	0.1 × 0.03 × 0.03	0.08 × 0.03 × 0.03	0.1 × 0.05 × 0.04	0.08 × 0.03 × 0.03	0.08 × 0.04 × 0.03
Reflections collected	10,884	8871	8866	8732	14,065
Independent reflections	1701 [*R*(int)=0.0455]	1721 [*R*(int)=0.0388]	1734 [*R*(int)=0.0333]	1744 [*R*(int)=0.0571]	1746 [*R*(int)=0.0492]
Completeness to theta=28.24 (%)	99.90	99.90	99.50	99.90	99.80
Data/restraints/parameters	1701/0/67	1721/0/73	1734/0/73	1744/0/72	1746/0/72
Goodness-of-fit on *F*2	1.913	1.078	1.082	1.059	1.114
Final *R* indices [$I > 2\sigma$ sigma(I)]	*R*1=0.0556, *wR*2=0.1310	*R*1=0.0319, *wR*2=0.0774	*R*1=0.0349, *wR*2=0.0792	*R*1=0.0467, *wR*2=0.1193	*R*1=0.0493, *wR*2=0.0975
Largest diff. peak and hole	4.765 and −3.348 e^{-3}	3.836 and −2.35 e^{-3}	3.91 and −2.873 e^{-3}	5.846 and −4.778 e^{-3}	2.942 and −3.985 e^{-3}

$R1=\Sigma||F_0|-|F_c||/\Sigma|F_0|$ $wR2=\{\Sigma(w(F_0^2-F_c^2)^2)/\Sigma(w(F_0^2)^2)\}^{1/2}$.

Table 2
Fractional Atomic Coordinates and Equivalent Isotropic Atomic Displacement Parameters (U_{eq}) in 10^{-3} (Å^2) and Site Occupancies for (a) $Sn_3Bi_2Se_6$, (b) $Sn_{3-\delta}Pb_\delta Bi_2Se_6$ (δ=0.1), (c) $Sn_{3-\delta}Pb_\delta Bi_2Se_6$ (δ=0.3), (d) $Sn_{3-\delta}Pb_\delta Bi_2Se_6$ (δ=0.5), and (e) $Sn_{3-\delta}Pb_\delta Bi_2Se_6$ (δ=0.7).

	Site	x	y	z	SOF	U_{eq}
(a)						
M1	4c	0.1409(1)	0.25	0.8288(1)	Bi/Sn [0.8/0.2]	7(1)
M2	4c	0.0490(1)	0.75	0.6102(1)	Bi/Sn [0.8/0.2]	7(1)
M3	4c	0.1251(1)	−0.25	0.3300(1)	Sn [100%]	10(1)
M4	4c	−0.0471(1)	0.75	0.8929(1)	Bi/Sn [0.3/0.7]	14(1)
M5	4c	0.2300(1)	0.75	0.0607(1)	Bi/Sn [0.1/0.9]	21(1)
Se6	4c	0.2574(1)	0.25	0.9232(1)		12(1)
Se7	4c	0.0860(1)	−0.25	0.4805(1)		7(1)
Se8	4c	0.1722(1)	−0.25	0.6928(1)		7(1)
Se9	4c	0.1066(1)	−0.25	0.9815(1)		8(1)
Se10	4c	0.0024(1)	0.25	0.7607(1)		6(1)
Se11	4c	0.1600(1)	0.25	0.1999(1)		6(1)
(b)						
M1	4c	0.3597(1)	0.25	0.1697(1)	Bi/Sn [0.812(7)/0.188]	18(1)
M2	4c	0.0496(1)	−0.75	−0.1119(1)	Bi/Sn [0.840(7)/0.160]	17(1)
M3	4c	0.1250(1)	0.25	0.1698(1)	Sn/Bi [0.936(6)/0.064]	16(1)
M4	4c	0.4528(1)	−0.75	−0.1045(1)	Sn/Bi [0.831(6)/0.169]	21(1)
M5	4c	0.2669(1)	−0.25	−0.0610(1)	Sn/Pb [0.814(7)/0.186]	34(1)
Se6	4c	0.2432(1)	0.25	0.0774(1)		20(1)
Se7	4c	0.0865(1)	−0.25	0.0182(1)		18(1)
Se8	4c	0.3288(1)	−0.25	0.3054(1)		18(1)
Se9	4c	0.3923(1)	−0.25	0.0187(1)		18(1)
Se10	4c	0.4965(1)	0.25	0.2378(1)		17(1)
Se11	4c	0.1593(1)	−0.25	0.3002(1)		16(1)
(c)						
M1	4c	0.3606(1)	0.25	0.1685(1)	Bi/Sn [0.797(8)/0.203]	20(1)
M2	4c	0.0495(1)	−0.75	−0.1117(1)	Bi/Sn [0.820(8)/0.18]	19(1)
M3	4c	0.1261(1)	0.25	0.1680(1)	Sn/Bi [0.884(7)/0.116]	17(1)
M4	4c	0.4521(1)	−0.75	−0.1070(1)	Sn/Bi [0.721(7)/0.279]	23(1)
M5	4c	0.2655(1)	−0.25	−0.0631(1)	Sn/Pb [0.677(8)/0.323]	38(1)
Se6	4c	0.2440(1)	0.25	0.0763(1)		23(1)
Se7	4c	0.0870(1)	−0.25	0.0180(1)		22(1)
Se8	4c	0.3294(1)	−0.25	0.3044(1)		19(1)
Se9	4c	0.3946(1)	−0.25	0.0175(1)		22(1)
Se10	4c	0.4972(1)	0.25	0.2406(1)		18(1)
Se11	4c	0.1603(1)	−0.25	0.2987(1)		19(1)
(d)						
M1	4c	0.2619(1)	0.25	0.1671(1)	Bi/Sn [0.718(5)/0.282]	17(1)
M2	4c	0.0497(1)	−0.75	−0.1118(1)	Bi/Sn [0.789(2)/0.211]	15(1)
M3	4c	0.1273(1)	0.25	0.1664(1)	Sn/Bi [0.804(3)/0.196]	17(1)
M4	4c	0.4515(1)	−0.75	−0.1087(1)	Sn/Bi [0.616(8)/0.384]	18(1)
M5	4c	0.2632(1)	−0.25	0.0649(1)	Sn/Pb [0.584(4)/0.416]	38(1)
Se6	4c	0.2451(1)	0.25	0.757(1)		17(1)
Se7	4c	0.0883(1)	−0.25	0.0175(1)		18(1)
Se8	4c	0.3303(1)	−0.25	0.3024(1)		14(1)
Se9	4c	0.3967(1)	−0.25	0.0168(1)		18(1)
Se10	4c	0.4977(1)	0.25	0.2427(1)		13(1)
Se11	4c	0.1614(1)	−0.25	0.2976(1)		14(1)
(e)						
M1	4c	0.3655(1)	0.25	0.1646(1)	Bi/Sn [0.492(1)/0.508]	21(1)
M2	4c	0.0498(1)	−0.75	−0.1117(1)	Bi/Sn [0.674(3)/0.326]	19(1)
M3	4c	0.1314(1)	0.25	0.1644(1)	Sn/Bi [0.579(7)/0.421]	25(1)
M4	4c	0.4505(1)	−0.75	−0.1114(2)	Sn/Bi [0.354(4)/0.646]	23(1)
M5	4c	0.2535(1)	−0.25	−0.0676(1)	Sn/Pb [0.334(1)/0.666]	63(1)
Se6	4c	0.2484(1)	0.25	0.0747(1)		24(1)
Se7	4c	0.0929(1)	−0.25	0.0160(1)		24(1)
Se8	4c	0.3328(1)	−0.25	0.2988(1)		18(1)
Se9	4c	0.4030(1)	−0.25	0.0157(1)		25(1)
Se10	4c	0.4994(1)	0.25	0.2481(1)		17(1)
Se11	4c	0.1649(1)	−0.25	0.2971(1)		18(1)

Karlsruhe, Eggenstein-Leopoldshafen, Germany (Fax: +49 7247 808 666; E-mail: crysdata@fiz.karlsruhe.de) on quoting the depository numbers CSD-421349, 421350, 421351, 421352, and 421353.

Table 3
Selected interatomic distances in Å for $Sn_{3-\delta}Pb_\delta Bi_2Se_6$ (δ=0.0–0.7).

X	0.0	0.1	0.3	0.5	0.7
M1–Se6	2.785(2)	2.792(2)	2.794(2)	2.798(2)	2.780(1)
M1–Se8 × 2	2.865(2)	2.877(3)	2.884(1)	2.889(1)	2.888(2)
M1–Se9 × 2	3.033(2)	3.024(1)	3.036(3)	3.043(2)	3.047(1)
M1–Se10	3.083(2)	3.067(1)	3.082(2)	3.086(2)	3.069(1)
M2–Se7 × 2	2.842(2)	2.860(2)	2.865(3)	2.875(3)	2.892(1)
M2–Se7	3.122(2)	3.179(1)	3.189(1)	3.227(3)	3.307(2)
M2–Se8	2.844(2)	2.834(1)	2.831(2)	2.828(1)	2.784(1)
M2–Se10 × 2	3.086(2)	3.098(1)	3.083(1)	3.076(2)	3.044(1)
M3–Se6	2.797(3)	2.825(1)	2.816(1)	2.815(1)	2.778(2)
M3–Se7 × 2	3.039(2)	3.060(2)	3.055(1)	3.054(2)	3.049(2)
M3–Se10	2.974(2)	3.024(2)	3.027(1)	3.043(1)	2.053(1)
M3–Se11 × 2	2.834(2)	2.848(1)	2.854(2)	2.738(2)	2.879(1)
M4–Se9 × 2	2.976(2)	2.984(1)	2.970(2)	2.963(1)	2.919(1)
M4–Se10 × 2	2.947(2)	2.982(2)	2.989(2)	3.001(2)	3.019(2)
M4–Se11	2.712(2)	2.728(1)	2.728(4)	2.738(2)	2.759(2)
M4–Se9	3.490(2)	3.513(2)	3.499(1)	3.487(3)	3.381(2)
M5–Se6 × 2	2.862(2)	2.868(2)	2.876(1)	2.884(2)	2.881(2)
M5–Se9	2.832(2)	2.893(1)	2.970(2)	3.071(2)	3.377(3)
M5–Se11 × 2	3.194(2)	3.239(1)	3.241(1)	3.258(2)	3.303(2)
M5–Se8 × 2	3.459(1)	3.451(2)	3.438(1)	3.429(3)	3.344(1)

2.3. Characterization

X-ray powder diffraction analysis of the products was performed using a Bragg–Brentano-type powder diffractometer (Bruker D8 Advance, operated at 40 kV and 40 mA, Cu $K\alpha$, λ=1.5418 Å). For phase identification, XRD data were collected over a 2θ range 5–90° with a step interval of 0.05°. The bond valence calculations were performed using valence bond approach with R_0 values of 2.59, 2.67, and 2.72 Å for Sn^{2+}, Pb^{2+}, and Bi^{3+}, respectively [33].

Energy dispersive spectra (SEM/EDX, Hitachi S-4700I High-Resolution Scanning Electron Microscope) were recorded for the cuboid crystalline samples. Semiquantitative EDS analysis of individual crystals of each reaction product confirmed the presence of Sn, Pb, Bi, and Se. Differential thermal analyzer (DTA) and thermogravimetry (TG) measurements were performed using a thermal analyzer (NETZSCH STA 409PC). The powder sample (approximately 30 mg) was placed in an alumina crucible; Al_2O_3 powder served as a reference sample. The sample was heated to 1273 K at 20 K/min under a constant flow of N_2.

2.4. Physical property measurements

Seebeck coefficients were measured on a cold-pressed bar ($1 \times 1 \times 5\,mm^3$) with a commercial thermopower measurement apparatus (MMR Technologies) over the temperature range 300–500 K under dynamic vacuum ($\sim 10^{-2}$ Torr). Constantan served as an internal standard and silver conductive paint was used to create electrical contacts. DC conductivity measurements were performed using a standard four-probe method with a homemade device under vacuum ($\sim 10^{-2}$ Torr) over the temperature range 100–300 K. Electrical contacts consisted of four copper wires attached to the bulk with silver glue. Samples were placed under vacuum in room temperature for at least 1 h to allow the silver glue to dry completely, which improved contact performance. To minimize the effects of grain boundaries in the crystalline powder on conductivity measurements, each cold-pressed sample was annealed at 773 K for 72 h before measurement.

2.5. Theoretical calculations

Self-consistent tight-binding linear muffin tin orbital (LMTO) calculations using the atomic spheres approximation (ASA) were

undertaken to investigate the electronic structures of these compounds. The density-function theory was applied with the local density approximation (LDA) [34–38]. The atomic radii used were 1.72, 1.63, and 1.22 Å for Sn, Bi, and Se, respectively. All *k*-space integrations were performed with the tetrahedron method on $16 \times 16 \times 8$ grids of unique *k* points in the first Brillouin zone. Within the Brillouin zone based on the primitive cell of $Sn_3Bi_2Se_6$, 288 irreducible *k* points were used. We analyzed the electronic structure by extracting information from the densities of states (DOS) and the curves for crystal-orbital Hamiltonian populations (COHP) [39]. To understand the effects of the *M*5 position and Pb concentration on the electronic structure, stability, and bonding of the as-synthesized compounds, two models were constructed of the electronic structure: (a) $Sn_3Bi_2Se_6$ with the cation sites assigned to Bi(*M*1, *M*2) and Sn(*M*3–*M*5) in space group *Pnma*, and with the fractional coordinate *x* of the *M*5 site ranging from *x*=0.225 to 0.25 (on the mirror plane); (b) $Sn_{3-\delta}Pb_\delta Bi_2Se_6$ (δ=0, 1, and 3) with varied assignments of metal sites. Details of the models are described in Table S1.

3. Results and discussion

3.1. Synthesis

$Sn_3Bi_2Se_6$ (**1**) was initially obtained from a reaction intended to synthesize "$Sn_5Bi_6Se_{14}$" through the solid-state method. Based on powder X-ray diffraction results, the product of the "$Sn_5Bi_6Se_{14}$" reaction yielded an unknown phase after a search of the JCPDF database. A cuboid-shaped crystal was selected for single-crystal X-ray diffraction measurements and the refined form ula $Sn_3Bi_2Se_6$ was determined. Subsequently, reactions of $Sn_{3-\gamma}Bi_{2+\gamma}Se_6$ ($0 \le \gamma \le 1$) were conducted to probe the possible phase using two temperature profiles of slow cooling as described above and a quench reaction at 1073 K. However, attempts to obtain the charge-balanced product $Sn_3Bi_2Se_6$ failed; the reaction product contained a mixture of $Sn_3Bi_2Se_6$ and $SnSe_2$ phases. Products of the other reactions contained the primary phase and impurities of $SnSe_2$ and $Sn_3Bi_2Se_6$. For reactions using the quenching process, products of reactions with $0 \le \gamma \le 0.62$ yielded similar powder X-ray patterns to $Sn_3Bi_2Se_6$ with a broad peak width, indicative of poor crystallinity, with which it was impossible to perform a single-crystal study. For the quaternary system, a series of reactions with $Sn_{3-\delta}Pb_\delta Bi_2Se_6$ ($0 \le \delta \le 2$) were performed to investigate the phase width under the same heating conditions specified above. Based on powder XRD measurements, pure phases were obtained when $0.1 < \delta < 0.7$ (Fig. S1a). The calculated lattice parameters *a* and *b* exhibited weak correlations with the percent Pb composition, while the lattice parameter *c* expanded as the concentration of Pb increased in the framework (Fig. S2). The effect of percent Pb composition on cell volume is shown in Fig. S1b, indicating that the cell volume varies from 1204.2(6) Å^3 for Sn_3Bi_2 Se_6 (δ=0) to 1230(2) for $Sn_{2.3}Pb_{0.7}Bi_2Se_6$ (δ=0.7). The PbSe impurity phase began to form when $\delta > 0.7$. Crystals from the δ=0.1, 0.3, 0.5, and 0.7 reactions were selected for single-crystal X-ray analysis.

3.2. Crystal structure

The crystal structures of compounds **1–5** are closely related to that of lillianite $Pb_3Bi_2S_6$. These as-synthesized phases contain four formulae per unit cell, with eleven crystallographically inequivalent sites: four with mixed-occupancy cations Sn^{2+}/Bi^{3+}, one with Sn^{2+}/Pb^{2+} or fully occupancy Sn^{2+}, and six with Se^{2-}. The structure is illustrated in Fig. 1 as a projection along the crystallographic *b*-axis (010). The structure contains two slabs of the same thickness that exhibit NaCl (311) tilt planes expanding along the *a*, *b* direction, which are connected by a Se6 atom to form a three-dimensional structure. The same structural feature exists in $KSn_5Bi_5Se_{13}$ [25] and $InSn_6BiSe_9$ [28], which contain similar NaCl(311)-type layer units. The lillianite phase $Pb_3Bi_2S_6$ also contains a metal site on the cell-twinning plane showing mirror symmetry. However, the *M*5 metal sites in the present selenides exhibit a zigzag array along the *c*-axis with glide symmetry. The coordination environments of the metal sites fall into two groups. (i) The *M*1–*M*4 sites are six-coordinate, with two types of distorted octahedral environments. The first type is a square pyramid having one short (~2.73 Å), four intermediate (2.92–3.02 Å), and one longer (~3.5 Å) bond trans to the shorter *M*–Se distances. The second type is a trigonal pyramid with three short *M*–Se bonds (2.7–2.9 Å) opposite to three longer ones (2.9–3.1 Å). (ii) The *M*5 site is close to the pseudo-mirror plane with zigzag arrays along the (001) direction, as shown in Fig. 1. Its coordination geometry can be described as a monocapped trigonal prism with *M*5–Se distances varying between 2.861(2) and 3.459(1) Å. The *M*–Se distances in both structures are comparable to those in a binary system and some multinary selenides in the literature that contain mixed occupancies of Bi/Sn or Pb/Sn, such as $Pb_4Sb_4Se_{10}$ [40], $Pb_{0.875}Sn_{0.125}Se$ [41], $PbBi_2Se_4$ [42], $InSn_2Bi_3Se_8$ [28], and $Sn_2Pb_5Bi_4Se_{13}$ [30].

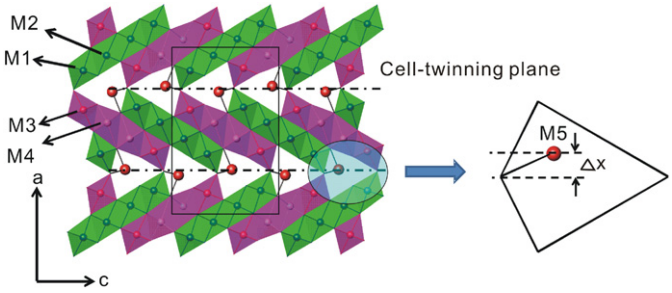

Fig. 1. Crystal structure of $Sn_{3-\delta}Pb_\delta Bi_2Se_6$ as a projection along the crystallographic *b*-axis [010]. The slabs exhibit NaCl (311) tilt planes and the atoms along the cell-twinning plane exhibit glide arrayal. Δx indicates the shift in position of the *M*5 atom from the cell-twinning plane.

The effect of Pb on electron density of the metal sites and the position of the *M*5 site was studied and the results are shown in Fig. 2. For ternary phase **1** and quaternary phases with a low Pb content, the refined electron count for metal sites fell into two groups with electrons ~78 (*M*1, *M*2) and ~55 e^-/site (*M*3, *M*4, *M*5), located in different NaCl(311) slab units (Fig. 1). As the Pb concentration was increased, electron densities of the *M*1 and *M*2 sites decreased, while those of the *M*3–*M*5 sites increased (Fig. 2a). The refined electron count of the metal sites regrouped to (*M*1, *M*3) and (*M*2, *M*4, *M*5) with ~55 and ~65 e^-/site, respectively, at the highest Pb concentration (**5**, δ=0.7). Fig. 2b shows the fractional coordinate *x* of the *M*5 sites in the structure of **1–5**. The results indicate that the *M*5 site gradually shifts to the cell-twinning plane at *x*=0.25 as the composition of Pb on *M*5 increases. The interatomic distance of *M*5–Se9 increased from 2.841(1) to 3.377(3) Å and the fractional coordinate *x* varied from 0.2300(1) for $Sn_3Bi_2Se_6$ to 0.2465(1) for $Sn_{2.3}Pb_{0.7}Bi_2Se_6$. Bond valence sum calculations (BVM) clearly indicated that the *M*5 site of the ternary and Pb-rich quaternary phases approximated the formal oxidation states of Sn^{2+} and Pb^{2+}. Because the single-crystal analysis suggested that the *M*5 sites are mixed occupied by Bi/Sn(major) and Pb(major)/Sn for ternary and Pb-rich compounds, respectively, the results of the BVM are consistent with the model for the mixed-occupancy *M*5 site. The other metal sites of compounds **1–5** had calculated valences between 2.89 and

3.40 (*M*1–*M*2, Bi-rich) and 2.17 and 2.50 (*M*3–*M*4, Sn-rich). Fig. 1 shows that the paired (*M*1, *M*3) and (*M*2, *M*4) sites are associated with the pseudo-mirror plane at x=0.25. For the Pb-rich phase, the position of the *M*5 site is close to x=0.25 and the electron densities of (*M*1, *M*3) and (*M*2, *M*4) were close. The structure may leads to a space group with a mirror plane, such as *Cmcm*, from single-crystal structural analysis.

3.3. Electronic structure

The effect of the *M*5 position along the *a*-axis was studied by varying the fractional coordinate x from 0.225 to 0.25. The relative total energy and ICOHP values for *M*5–Se as a function of x are shown in Fig. 3. For relative total energies, the results suggest that the model stabilizes when the x value is shifted away from x=0.25. The most stable model is for x=0.2425, which is close to the observed value of 0.2465 for $Sn_{2.3}P_{0.7}Bi_2Se_6$. When $x < 0.2425$, the repulsive interaction between *M*5 and Se dominates and the total energy becomes unstable. The calculated ICOHP values can be treated as an index for the interatomic bonding strength; the results shown in Fig. 3 indicate that the interatomic interactions of the *M*5–Se contacts gradually increased until x=0.23. The results also suggest that the structure is more stable when the *M*5 site is shifted away from the mirror plane. Because the model considers only *M*5–Se bonding, the observed trend for the *M*5–Se contacts is not the same as the results of the total energy analysis. The results for the total energy and bonding character of *M*5–Se clearly demonstrate that the favored position of *M*5 is above or below the cell-twinning plane of the lillianite structure, which indicates why the space group *Pnma* was chosen rather than *Cmcm*.

The effect of substituting Sn for Pb atoms on the bonding character of the *M*5–Se contact was also studied (Fig. 4). In general, as seen from the DOS curve, the valence band was filled for all models with small band gaps (~0.4 eV), indicative of semiconducting behavior. Crystal-orbital Hamiltonian population (COHP) calculations indicate that the bonding states of the (Sn, Pb, Bi)–Se contacts were occupied and well below the Fermi level, with small contributions of antibonding interactions near the Fermi level (Fig. S3). The large peak between −5 eV and the Fermi level was dominated by the Se *p* orbital, whereas the bottom of the conduction band was mainly associated with empty *p* orbitals of the main-group metal. The *ns* states of the Sn, Pb, and Bi atoms were essentially localized and appeared as sharp peaks centered between −5 and −10 eV, likely resulting from the inert-pair effect commonly observed for heavy main-group elements. Further examination of the PDOS curves indicated that the Sn states decreased as the cation sites became gradually replaced with Pb. The projected densities of states (PDOS) for the *M*5 site (Fig. 4) exhibited sharp contributions of Sn(5*s*) states between −7.5 and −8.5 eV for the *M*5 site in $Sn_3Bi_2Se_6$, reduced by ~1 eV in the $Sn_2Pb_1Bi_2Se_6$ and $Pb_3Bi_2Se_6$ models in which the *M*5 site was occupied by Pb. The COHP curves for the *M*5–Se contacts (Fig. S3) show differences in the bonding characters of Pb–Se and Sn–Se. The results indicate that the *M*5–Se bonding states were shifted to a lower energy region due to the strong interaction of the Pb–Se contact. The results are consistent with experimental findings that the quaternary phase $Sn_{3-\delta}Pb_\delta Bi_2Se_6$ can be synthesized, while the pure ternary phase $Sn_3Bi_2Se_6$ is difficult to synthesize.

3.4. Physical properties

A standard four-probe technique was used to measure temperature-dependent resistivity from 100 to 300 K. Compounds **1**–**5** exhibited decreasing resistivity with increasing temperature, consistent with the typical trend for semiconducting property (Fig. 5a). Compounds **1**–**5** had negative and nearly temperature-independent thermopower and the maximum observed at δ=0.5, indicative of n-type semiconducting behavior in which the majority of the charge carriers are electrons (Fig. 5b). Room-temperature thermopower values are **1**: −53.2 μV/K, **2**: −116.8 μV/K, **3**: −77.9 μV/K, **4**: −148.2 μV/K, and **5**: −128.4 μV/K, which are too small for thermoelectric applications.

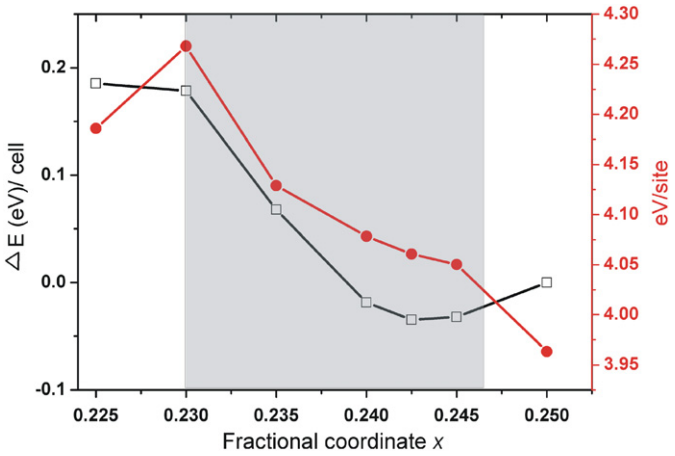

Fig. 3. Theoretical calculations for the $Sn_3Bi_2Se_6$ model vs. the fractional coordinate x of the *M*5 sites. The black line is the difference in total energy; the energy at x=0.25 was set to zero for this curve. The blue line shows the ICOHP for the *M*5 atom vs. fractional coordinate x. The gray area corresponds to single-crystal results for the $Sn_{3-\delta}Pb_\delta Bi_2Se_6$ (δ=0.0–0.7) system.

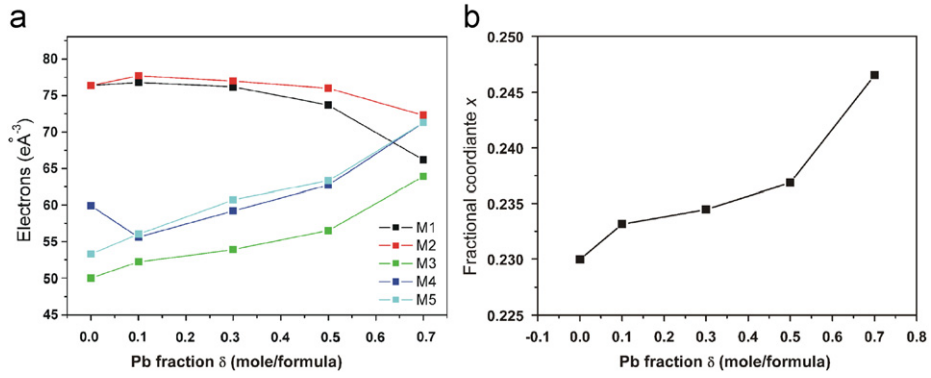

Fig. 2. Electronic distributions at the five cation sites (a) and variations with the fractional coordinate x of the *M*5 site (b) in the $Sn_{3-\delta}Pb_\delta Bi_2Se_6$ (δ=0.0–0.7) systems. The standard deviations are smaller than the symbols shown.

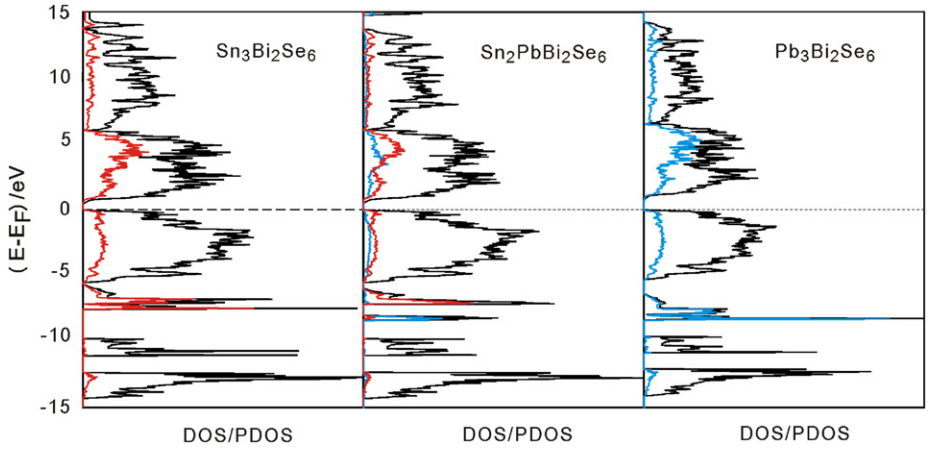

Fig. 4. Densities of states and partial densities of states for selected *M*–Se bonds (Sn: red line, Pb: blue line, total DOS: black line) for the $Sn_3Bi_2Se_6$ (left), $Sn_2PbBi_2Se_6$ (middle) and $Pb_3Bi_2Se_6$ (right) models. The horizontal dashed line denotes the Fermi energy (E_F).

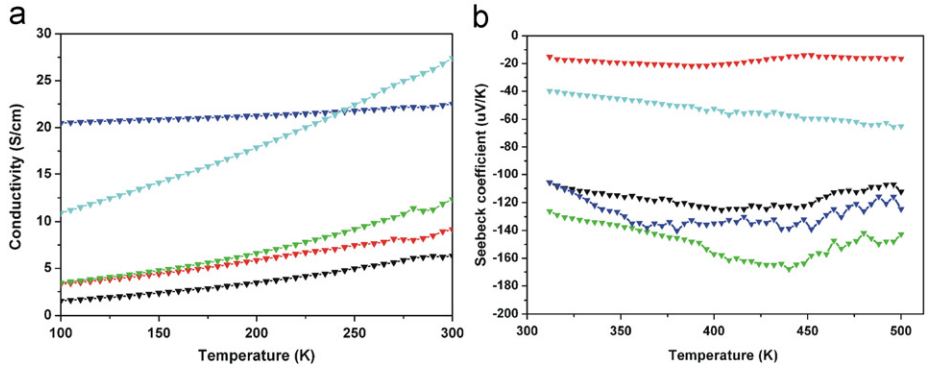

Fig. 5. Temperature dependence of electrical conductivity (a) and thermoelectric power (b) of $Sn_{3-\delta}Pb_\delta Bi_2Se_6$ for δ=0.0 (light blue), δ=0.1 (black), δ=0.3 (red), δ=0.5 (green), and δ=0.7 (dark blue).

3.5. Thermoanalyses

The TG–DTA vs. temperature curve for compound **1** exhibited maximum exothermic peaks at 972 K, corresponding to decomposition of the compound near 1082 K. The quaternary compounds **2**–**5** had similar results with increased exothermic and decomposition peaks at ~1007 and ~1093 K, respectively (Fig. S4). These results were reproduced by heating the as-synthesized powder in a quartz ampoule under vacuum and subsequently heating to 1173 K. The PXRD pattern of the residual product was indexed as a mixture of $SnSe_2$, Bi_2Se_3, PbSe, and Se phases.

4. Conclusions

This study presents combined experiments and calculations to investigate site preference in the crystal structures of $Sn_{3-\delta}Pb_\delta Bi_2Se_6$ (δ=0.0–0.7). The quaternary selenides $Sn_{3-\delta}Pb_\delta Bi_2Se_6$ (δ=0.1–0.7) contained various amounts of Pb, which affected not only the electron density but also the position of the metal sites. All compounds were n-type semiconductors with small band gaps as confirmed by measurements of physical properties and calculation of electronic structures.

Acknowledgment

The National Science Council (NSC94-2113-M-009-012, 94-2120-M-009-014) supported this research.

Appendix A. Supplementary materials

Supplementary data associated with this article can be found in the online version at doi:10.1016/j.jssc.2010.01.011

References

[1] T.J. McCarthy, M.G. Kanatzidis, Inorg. Chem. 34 (1995) 1257.
[2] L. Iordanidis, D. Bilic, S.D. Mahanti, M.G. Kanatzidis, J. Am. Chem. Soc. 125 (2003) 13741.
[3] K.S. Choi, D.Y. Chung, A. Mrotzek, P. Brazis, C.R. Kannewurf, C. Uher, W. Chen, T. Hogan, M.G. Kanatzidis, Chem. Mater. 13 (2001) 756.
[4] J.H. Liao, G.A. Marking, K.F. Hsu, Y. Matsushita, M.D. Ewbank, R. Borwick, P. Cunningham, M.J. Rosker, M.G. Kanatzidis, J. Am. Chem. Soc. 125 (2003) 9484.
[5] M. Tampier, D. Johrendt, J. Solid State Chem. 158 (2001) 343.
[6] J.O. Sofo, G.D. Mahan, Phys. Rev. B 49 (1994) 4565.
[7] F.J. DiSalvo, Science 285 (1999) 703.
[8] M.G. Kanatzidis, Semicond. Semimet. 69 (2001) 51.
[9] J. Takagi, Y. Takeuchi, Acta Crystallogr. Sect. B: Struct. Sci. 28 (1972) 649.
[10] E. Makovicky, S. Karup-Moeller, Neues Jahrb. Mineral. Abh. 131 (1977) 56.
[11] B.G. Hyde, S. Andersson, M. Bakker, C.M. Plug, M. O'Keeffe, Prog. Solid State Chem. 12 (1980) 273.
[12] S. Misra, H.C. Padhi, J. Appl. Phys. 75 (1994) 4576.
[13] C.D. Lokhande, V.S. Yermune, S.H. Pawar, J. Electrochem. Soc. 138 (1991) 624.
[14] M.G. Kanatzidis, Acc. Chem. Res. 36 (2003) 111.
[15] M.G. Kanatzidis, Acc. Chem. Res. 38 (2005) 359.
[16] Y. Takeuchi, J. Takagi, T. Yamanaka, Proc. Jpn. Acad. 50 (1974) 317.
[17] M. Ohmasa, W. Nowacki, Z. Kristallogr. 137 (1973) 422.
[18] M. Ohmasa, Neues Jahrb. Mineral. Monatsh. (1973) 227.
[19] J.H. Kim, D.Y. Chung, D. Bilc, S. Loo, J. Short, S.D. Mahanti, T. Hogan, M.G. Kanatzidis, Chem. Mater. 17 (2005) 3606.
[20] L.A. Olsen, T. Balić-Zunić, E. Makovicky, Inorg. Chem. 47 (2008) 6756.
[21] K. Bente, M. Engel, M. Steins, Z. Kristallogr. 205 (1993) 327.
[22] H. Sawada, I. Kawada, E. Hellner, M. Tokonami, Z. Kristallogr. 180 (1987) 141.

[23] E. Makovicky, W.G. Mumme, I.C. Madsen, Neues Jahrb. Mineral. Abh. 10 (1992) 454.
[24] Y. Takeuchi, J. Takagi, Proc. Jpn. Acad. 50 (1974) 76.
[25] A. Mrotzek, M.G. Kanatzidis, Inorg. Chem. 42 (2003) 7200.
[26] H.K. Herbert, W.G. Mumme, Neues Jahrb. Mineral. Abh. (1981) 69.
[27] S. Karup-Moller, E. Makovicky, Bull. Geol. Soc. Den. 26 (1977) 41.
[28] M.F. Wang, S.M. Jang, J.C. Huang, C.S. Lee, J. Solid State Chem. 182 (2009) 1450.
[29] M.F. Wang, W.H. Huang, C.S. Lee, Inorg. Chem. 48 (2009) 6402.
[30] K.B. Chen, C.S. Lee, Solid State Sci. 11 (2009) 1666.
[31] SAINT Version 6.22, Siemens Analytical X-ray Instruments Inc., Madison, WI, 2001.
[32] SHELXTL Version 6.10, Reference Manual; Siemens Analytical X-Ray Systems, Inc., Madison, WI, 2000.
[33] U.D. Altermatt, I.D. Brown, Acta Crystallogr. Sect. A: Found. Crystallogr. 43 (1987) 125.
[34] O.K. Andersen, Phys. Rev. B 12 (1975) 3060.
[35] H.L. Skriver, The LMTO Method, Springer, Berlin, 1984.
[36] U. van Barth, L. Hedin, J. Phys. C 4 (1971) 2064.
[37] P.E. Blöhl, O. Jepsen, O.K. Andersen, Phys. Rev. B 49 (1994) 16223.
[38] O. Jepsen, O.K. Andersen, Z. Phys. 97 (1995) 25.
[39] R. Dronskowski, P.E. Blöhl, J. Phys. Chem. 97 (1993) 8617.
[40] A. Skowron, I.D. Brown, Acta Crystallogr. Sect. C 46 (1990) 2287.
[41] S.V. Ovsyannikov, V.V. Shchennikov, A.Y. Manakov, A.Y. Likhacheva, I.F. Berger, A.I. Ancharov, M.A. Sheromov, Phys. Status Solidi B 244 (2007) 279.
[42] K.A. Agaev, S.A. Semiletov, Kristallografiya 13 (1968) 258.